Nanoscale
Advances

PAPER

View Article Online
View Journal | View Issue

Cite this: *Nanoscale Adv.*, 2025, **7**, 7182

Structure–property–performance correlation in $BiVO_4$ photoanodes synthesized by intensity-tuned pulse electrodeposition

Nguyen Thi Huyen,[abc] Thi Viet Ha Luu,[d] Tran Le[ab] and Huu Phuc Dang[*e]

The development of efficient and stable photoanodes is critical for advancing photoelectrochemical (PEC) water splitting technologies. In this work, bismuth vanadate ($BiVO_4$) photoanodes were fabricated using a two-step method combining the pulse electrodeposition of bismuth and spin-coating of a vanadium precursor [$VO(acac)_2$], followed by thermal annealing. By systematically varying the pulse voltages and vanadium precursor volume, a series of samples were produced. The sample labeled Bi-576 (deposited at 1.5–1.7 V with 0.6 μL $VO(acac)_2$) exhibited the highest PEC performance. This optimized sample achieved a photocurrent density of 1.33 mA cm^{-2} at 1.23 V *vs.* RHE, with an applied bias photon-to-current efficiency (ABPE) of 20% and a charge injection efficiency of 60.1% under AM 1.5G illumination. Structural analysis *via* X-ray diffraction revealed a preferential (121) crystal orientation and reduced crystallite size, promoting directional charge transport and suppressing recombination. Raman and X-ray photoelectron spectroscopy confirmed the presence of Bi^{3+}, V^{5+}, and strong V–O bonding, along with surface oxygen species that enhance charge separation and interfacial transfer. Field-emission scanning electron microscopy showed a porous, interconnected morphology that increased the electrochemical active surface area (ECSA). Electrochemical impedance spectroscopy and Mott–Schottky analysis revealed a high donor density of 8.65×10^{20} cm^{-3} and a long interfacial time constant (τ_{int}) of 31.46 ms, both contributing to efficient charge transport. Stability tests showed that Bi-576 retained over 82% of its photocurrent after 10 hours of continuous operation, indicating excellent long-term durability. These results demonstrate that tuning the pulse deposition conditions and precursor chemistry enables the rational design of $BiVO_4$ photoanodes with optimized structural and electronic properties. This scalable approach offers a promising route for the development of high-performance photoanodes for solar-driven water splitting.

Received 9th July 2025
Accepted 12th September 2025

DOI: 10.1039/d5na00667h

rsc.li/nanoscale-advances

Introduction

The increasing global demand for sustainable and renewable energy sources has led to significant research efforts in the field of photoelectrochemical (PEC) water splitting, a process that uses solar energy to convert water into hydrogen and oxygen.[1] Hydrogen is regarded as one of the most promising clean energy carriers owing to its high energy content and ability to be produced without generating greenhouse gases.[2,3] Among the various materials investigated for PEC water splitting, bismuth vanadate ($BiVO_4$) has emerged as a promising photoanode material because of its suitable bandgap (2.4 eV), low toxicity, and high chemical stability under photoelectrochemical conditions.[4] However, the efficiency of $BiVO_4$ as a photoanode is limited by its relatively poor charge-separation efficiency and slow water-oxidation kinetics.[5] Therefore, developing an efficient synthesis method for $BiVO_4$ thin films with desirable structural and electronic properties is crucial for improving PEC water splitting performance. One effective way to overcome these limitations is to engineer the $BiVO_4$ thin film structure at both the bulk and interface levels, for example, through surface passivation and cocatalyst engineering strategies that have been shown to suppress interfacial recombination and boost PEC performance.[6,7] In this context, developing a synthesis approach that offers precise control over morphology and crystallinity is crucial for improving charge transport and interfacial catalytic activity.

Electrodeposition has emerged as a cost-effective, scalable, and versatile technique for fabricating metal oxide photoanodes, including $BiVO_4$. Compared to other solution-based or vacuum-based methods, electrodeposition enables direct growth on

---

[a] *Faculty of Physics & Engineering Physics, VNUHCM-University of Science, Ho Chi Minh City, Vietnam*
[b] *Vietnam National University Ho Chi Minh City, Ho Chi Minh City, Vietnam*
[c] *Faculty of Physics, Ho Chi Minh City University of Education, Ho Chi Minh City, Vietnam*
[d] *Faculty of Chemical Engineering, Industrial University of Ho Chi Minh City, Ho Chi Minh City, Vietnam*
[e] *Faculty of Fundamental Science, Industrial University of Ho Chi Minh City, Ho Chi Minh City, Vietnam. E-mail: danghuuphuc@iuh.edu.vn*

conductive substrates, good film adhesion, and tunable microstructure through control of deposition parameters.[8,9] Importantly, the electrodeposition process can influence not only the thickness and porosity of the film but also the grain connectivity and defect density, which are closely linked to the charge separation and transport properties of $BiVO_4$. Therefore, optimizing the electrodeposition conditions represents a promising strategy to tailor the structural and electronic properties of $BiVO_4$ for enhanced PEC water splitting performance. Two common techniques employed in electrodeposition are direct current (DC) and pulsed current (PC) electrodepositions. Both methods have unique characteristics that influence the growth mechanism of the deposited material and the performance of the $BiVO_4$ film in PEC applications. DC electrodeposition involves applying a constant current to an electrolyte solution, resulting in the continuous deposition of the desired material onto the substrate. This method is relatively simple and easy to control but can lead to the formation of films with non-uniform grain sizes, high internal stress, and poor adhesion, particularly when the deposition rate is too high.[10] These issues may negatively impact the crystallinity, surface area, and charge-carrier mobility of the resulting $BiVO_4$ film. In contrast, pulse-current (PC) electrodeposition involves applying current pulses at regular intervals, allowing for control of both the on-time and off-time of the current.[11] This technique enables a more controlled nucleation and growth process, leading to films with finer grain sizes, reduced internal stress, and better mechanical properties than the DC-deposited films.[12,13] PC electrodeposition also offers the advantage of better control over the composition and morphology of the film, which is crucial for optimizing PEC performance. Several studies have explored the influence of deposition parameters such as pH, temperature, and precursor concentration on the PEC performance of $BiVO_4$ films.[14] However, a direct comparison of the growth mechanisms and PEC performance of $BiVO_4$ films deposited using DC and PC electrodeposition methods has not been thoroughly investigated. Such a comparative study would provide valuable insights into the advantages and limitations of each technique and could aid in optimizing the electrodeposition process for synthesizing high-performance $BiVO_4$ photoanodes.

In this study, we present a comparative analysis of the growth and PEC performance of $BiVO_4$ films synthesized using DC and PC electrodeposition. The primary objective of this study is to understand how different deposition techniques influence the structural, morphological, and electrochemical properties of $BiVO_4$ films and how these properties affect the ability of the films to function as photoanodes in PEC water splitting. We hypothesized that PC electrodeposition, with its controlled nucleation and growth processes, would yield $BiVO_4$ films with superior morphology and electrochemical properties compared to DC-deposited films, leading to enhanced PEC performance.

Experimental section

Materials

All reagents used in the experiment, including bismuth nitrate $Bi(NO_3)_3 \cdot 5H_2O$, acetylacetone vanadium [$VO(acac)_2$], dimethyl sulfoxide (DMSO), NaOH, and HNO_3, were purchased from Sinopharm Chemical Reagent Co., Ltd (Shanghai, China). The fluorine-doped tin oxide (FTO) substrate (TEC-7, 6–9 $\Omega\ sq^{-1}$, 1 × 2 cm) was ultrasonically cleaned sequentially with acetone, absolute alcohol, and deionized water for 30 min before being used.

Fabrication of $BiVO_4$ photoanodes

The $BiVO_4$ photoanodes were synthesized *via* a two-step process: electrochemical deposition of Bi, followed by spin-coating of the vanadium precursor and annealing, as shown in Scheme 1. The FTO substrates were sequentially cleaned with acetone, ethanol, and deionized water *via* ultrasonic treatment for 10 min each and then dried under a nitrogen flow. A 0.25 M $Bi(NO_3)_3$ aqueous solution (pH adjusted to 2 using HNO_3) was prepared and sonicated for 1 h. Electrodeposition was performed in a three-electrode cell with FTO as the working electrode, a Pt mesh counter electrode, and Ag/AgCl (3 M KCl) as the reference electrode. Pulse electrodeposition was performed using the following voltage sequences: 1.5–1.3 V (Bi536), 1.5–1.5 V (Bi574), 1.5–1.7 V (Bi576), and constant 1.5 V for the DC sample (Bi5DC). The pulse conditions employed a duty cycle of 1 s "on" and 1 s "off" for 20 min at room temperature. A 0.2 M $VO(acac)_2$ solution in DMSO was spin-coated onto the deposited Bi films. Two precursor volumes (0.4 and 0.6 μL) were tested. The films were then annealed in ambient air at 400 °C for 2 h (ramp rate: 10 °C min^{-1}). During annealing, Bi and V reacted to form crystalline $BiVO_4$. Residual vanadium oxides were removed by immersing the samples in 0.1 M NaOH for 10 min, followed by rinsing with deionized water and air drying. The samples were labeled according to the electrodeposition parameters and precursor volume. For example, Bi-576 refers to a sample pulsed at 1.5–1.7 V with 0.6 μL of $VO(acac)_2$.

Material characterization

The crystal structure of the $BiVO_4$ photoanodes was investigated using X-ray diffraction (XRD, Bruker D8 Advance) equipped with a Cu Kα radiation source ($\lambda = 1.5406$ Å) operating at 40 kV and 40 mA. Diffraction patterns were recorded over the 2θ range of 10–60° at a scan rate of 0.02° s^{-1}. Raman spectroscopy was

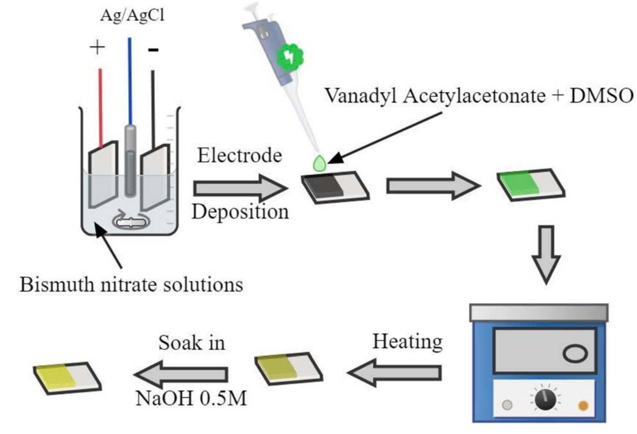

Scheme 1 Fabrication of $BiVO_4$ photoanodes.

conducted on a Horiba LabRAM HR Evolution system with a 532 nm laser source and a spectral resolution of 1 cm^{-1} to assess vibrational modes and phase purity. Field-emission scanning electron microscopy (FESEM, Hitachi S-4800) was used to observe the surface morphology and uniformity of the films. The elemental distribution was analyzed using energy-dispersive X-ray spectroscopy (EDX) coupled with FESEM. UV-Vis diffuse reflectance spectra were obtained using a Shimadzu UV-2600 spectrophotometer equipped with an integrating sphere attachment. The bandgap energies were estimated using the Tauc plot method for indirect allowed transitions. The incident photon-to-current efficiency (IPCE) was measured using a quantum efficiency system (PEC-S20, Peccell Technologies) under monochromatic light illumination. A 150 W Xe lamp equipped with a monochromator was used as the light source. Gas evolution measurements for hydrogen and oxygen were performed using a water displacement method under AM 1.5G illumination (100 mW cm^{-2}) at 1.23 V *vs.* RHE in 0.5 M Na_2SO_4 (pH $\sim$ 6.5). The evolved gases were collected from a sealed PEC cell with a quartz window and quantified at defined time intervals using a gas-tight syringe connected to a gas burette. The molar ratio of H_2 to O_2 was monitored to evaluate the faradaic efficiency and stoichiometric consistency.

Photoelectrochemical (PEC) measurements

PEC performance was evaluated using a three-electrode configuration in 0.5 M Na_2SO_4 electrolyte (pH $\approx$ 6.8) under AM 1.5G simulated sunlight (100 mW cm^{-2}, Newport solar simulator). The $BiVO_4$ photoanode served as the working electrode, a platinum mesh as the counter electrode, and Ag/AgCl (3 M KCl) as the reference electrode. All potentials were converted to the reversible hydrogen electrode (RHE) using the Nernst equation. Linear sweep voltammetry (LSV) was performed from 0 to 1.5 V *vs.* RHE at a scan rate of 10 mV s^{-1} under chopped light. Electrochemical impedance spectroscopy (EIS) was performed in the frequency range of 0.1 Hz to 100 kHz with a perturbation amplitude of 10 mV at 1.23 V *vs.* RHE. Transient photocurrent measurements were conducted under chopped illumination (light on/off intervals of 10 s) at 1.23 V *vs.* RHE. Mott–Schottky plots were obtained at a frequency of 1 kHz to estimate flat-band potentials and donor densities.

The applied bias photon-to-current efficiency (ABPE) was calculated using the following equation:

$$\mathrm{ABPE}\ (\%) = 100 \times \frac{J \times (1.23 - V_{\mathrm{bias}})}{P_{\mathrm{light}}} \tag{1}$$

where J is the photocurrent density (mA cm^{-2}), V_{bias} is the applied bias *vs.* RHE, and $P_{\mathrm{light}} = 100$ mW cm^{-2}.

Results and discussion

X-ray diffraction (XRD) analysis (Fig. 1) was performed to evaluate the crystallographic structure and phase composition of the synthesized films. The diffraction patterns revealed peaks corresponding to both SnO_2 from the FTO substrate and monoclinic scheelite $BiVO_4$ (JCPDS PDF#14-0688).[15] $BiVO_4$ peaks at 2-theta values of 18.8°, 28.9°, 30.8°, 33.5°, 40.1°, 42.4°, 45.7°, 47.3°, and 53.4°, corresponding to the (*hkl*) planes (110), (011), (121), (040), (200), (211), (150), (204), (224), and (116), respectively.[16] The prominent peak at 28.9°, indexed to the (121) plane, was dominant in all the samples, indicating a preferential orientation. This plane facilitates efficient interaction

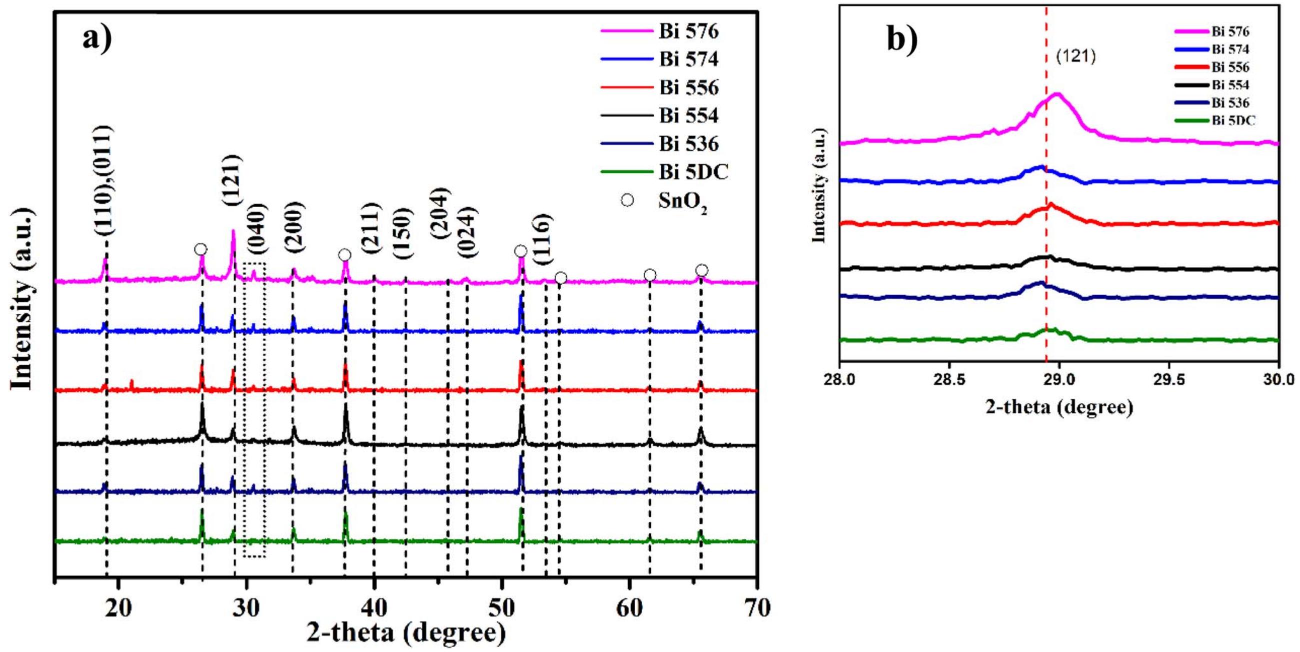

Fig. 1 (a) X-ray diffraction (XRD) patterns of Bi5DC, Bi536, Bi554, Bi556, Bi574, and Bi576 photoanodes and SnO_2. (b) XRD patterns of photoanodes in the 2θ range of 28°–30°.

between the photoanode and water molecules, critical for enhancing PEC performance.[17] The intensity ratio of the (121) to (040) planes varied depending on the fabrication conditions, with the highest ratio observed for the Bi576 sample. The high intensity of the (121) plane in Bi-576 indicates a preferential orientation, which facilitates anisotropic charge transport pathways in the $BiVO_4$ crystal lattice. This orientation reduces bulk recombination by aligning the crystal structure with the direction of the photogenerated carrier flow. Such alignment is beneficial for PEC performance, as supported by the higher photocurrent density observed for Bi-576.

The average crystallite size of the samples was calculated using the Scherrer equation:[18]

$$\tau = \frac{K\lambda}{\beta\cos(\theta)} \tag{2}$$

where τ is the average crystallite size, K is the dimensionless shape factor (approximately equal to unity), λ is the wavelength of X-rays, β is the line broadening at half the maximum intensity (FWHM), and θ is the Bragg angle.

The full width at half maximum (FWHM) analysis using the Scherrer equation revealed that Bi-576 possessed smaller crystallite domains (~54.3 Å) compared to Bi-552 (~367.2 Å), suggesting a higher density of grain boundaries that can facilitate charge separation. Although the FESEM images revealed larger aggregated particles, the smaller XRD-derived crystallites indicated a polycrystalline character within individual particles, contributing to enhanced PEC activity. The smaller crystallite size of Bi576 is attributed to the optimized deposition conditions, which enhance the nucleation rate and result in finer-grained structures. These findings highlight the significant role of crystallinity and preferred orientation in determining the PEC performance of the $BiVO_4$ photoanodes in general. The strong (121) peak intensity and reduced crystallite size of Bi576 contributed to its superior photocatalytic properties by enhancing charge separation and reducing recombination losses. The Bi5DC sample, which corresponds to five deposition layers and has a lower intensity at the diffraction peaks, shows the largest average crystallite size of approximately 367.2 Å. On the other hand, samples under different deposition conditions had smaller crystallite sizes, which were 367.2, 119.4, 85.3, 99.5, and 54.3 Å for Bi536, Bi554, Bi556, Bi574, and Bi576, respectively.

Raman spectroscopy was used to investigate the bonding structure and phase composition of the $BiVO_4$ films. Fig. 2 shows the Raman spectra with characteristic peaks at 202, 322, 356, 709, and 817 cm^{-1}, confirming the presence of the monoclinic scheelite phase.[19,20] Among these, the most prominent peak at 817 cm^{-1} is attributed to the symmetric stretching vibrations of the V–O bond within the VO_4 tetrahedra, a signature of the photoactive phase of $BiVO_4$.[19] The peak at 202 cm^{-1} corresponds to external lattice vibrations,[21] while the peaks at 322 and 356 cm^{-1} are associated with asymmetric and symmetric bending modes of the VO_4 unit.[22] The peak at 709 cm^{-1} is attributed to the asymmetric V–O stretching. Nikam and Joshi[21] reported that the monoclinic phase is a superior photocatalyst compared to the tetragonal phase because it can react thermodynamically and is more stable.

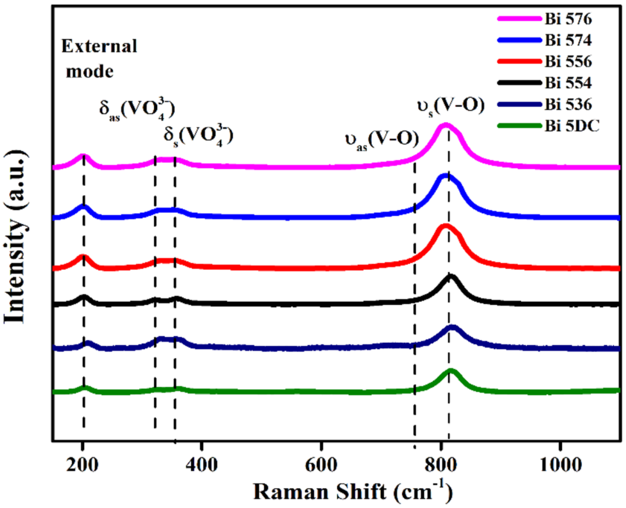

Fig. 2 Raman spectra of Bi5DC, Bi536, Bi554, Bi556, Bi574, and Bi576 photoanodes.

The equation expresses the relationship between the metal and oxygen bond lengths, and the Raman vibrational frequency is as follows:[23]

$$\nu\ (\mathrm{cm}^{-1}) = 21349 \times 10^{-1{,}9176\mathrm{R}(\text{Å})} \tag{3}$$

Here, ν corresponds to the Raman frequency of the symmetric stretching mode (Ag) of the V–O bond, and R is the V–O bond length.

Among all the samples, Bi576 exhibited the highest intensity and a noticeable blue-shift of the 817 cm^{-1} peak, indicating a shorter V–O bond length and improved phase purity. This shift implies a stronger orbital overlap between the V and O atoms, which can enhance the electronic conductivity. The increased Raman intensity further suggests enhanced crystallinity and fewer structural defects, leading to reduced trap states and improved carrier lifetimes in the films. These vibrational enhancements are attributed to the optimized pulse electrodeposition parameters used for Bi576, such as the precise pulse duration and current modulation. These conditions likely facilitated uniform nucleation and preferential formation of the monoclinic scheelite phase. The improved bonding structure directly supports a higher charge carrier mobility and reduces the electron–hole recombination, as reflected in the superior PEC performance of the Bi576 sample. Overall, Raman analysis confirmed that Bi-576 possesses a highly ordered and electronically favorable structure, reinforcing its role as the most efficient photoanode among the samples studied.

Diffuse reflectance spectroscopy (DRS) was employed to investigate the optical absorption characteristics and estimate the bandgap energy (E_g) of the $BiVO_4$ films (Fig. 3). This technique measures the intensity of light reflected from a sample irradiated with a broad-spectrum light source and provides insights into the electronic excitation processes in

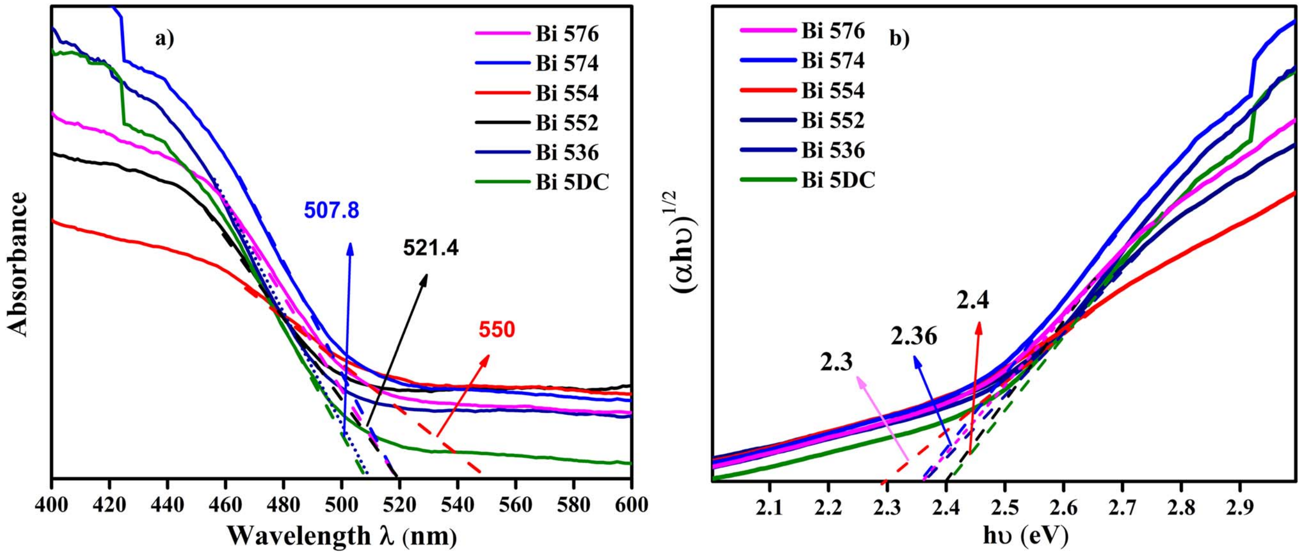

Fig. 3 (a) Absorption spectra and (b) bandgap width of Bi-5DC, Bi-536, Bi-554, Bi-556, Bi-574, and Bi-576 photoanodes.

semiconductors. The optical bandgap (E_g) was calculated using the Tauc plot method, which is based on the relationship between the absorption coefficient (α) and the photon energy ($h\nu$), as described by the Wood and Tauc model:[24]

$$\alpha = \frac{\alpha_0 (h\nu - E_g)^n}{h\nu} \tag{4}$$

where α is the absorption coefficient, $h\nu$ is the photon energy, α_0 and h are constants, E_g is the band's bandgap energy, and n is related to the nature of the electronic transition, depending more on the material type. For the semiconductor $BiVO_4$, n equals 1/2 in the above expression.[22,25]

The E_g values determined for Bi554, Bi574, Bi552, Bi576, and Bi556 were 2.30, 2.39, 2.40, 2.44, and 2.41 eV, respectively. These results indicate that all samples exhibit electronic transitions in the visible region, which is consistent with the requirements for efficient solar light absorption in PEC applications. Notably, Bi576 exhibited the widest bandgap (2.44 eV), which correlates with its enhanced crystallinity and improved structural order, as confirmed by XRD and Raman analyses. These bandgap values are in good agreement with previously reported results for $BiVO_4$ photoanodes synthesized *via* electrochemical and hydrothermal techniques.[26,27] The slight bandgap variations across the samples reflect subtle differences in the microstructure and stoichiometry influenced by the pulse electrodeposition parameters, which ultimately impact the charge carrier generation and separation efficiencies.

Field-emission scanning electron microscopy (FESEM) images (Fig. 4) were used to evaluate the morphology of the $BiVO_4$ samples synthesized *via* electrochemical deposition. The surface morphology of the bismuth metal (Bi55) film (Fig. 4a) exhibits a complex wavy network structure with loosely packed layers and uneven thickness, indicating uncontrolled nucleation owing to suboptimal pulse parameters. In contrast, the bismuth metal (Bi57) film (Fig. 4b) shows a denser fibrous network, where small clusters are more uniformly distributed and have well-defined edges. This improved morphology reflects the enhanced control over nucleation and grain growth achieved by tuning the pulse deposition conditions. These results highlight the effectiveness of pulse electrodeposition in modulating the structural evolution of the film. Distinct morphological changes were observed across the samples upon conversion to $BiVO_4$ *via* spin-coating $VO(acac)_2$ and thermal annealing. At lower vanadium precursor volumes (*e.g.*, Bi554 and Bi556), the surfaces appeared smoother and more branched, suggesting partial reactions and moderate grain interconnections. Increasing the $VO(acac)_2$ volume, as in Bi574 and Bi576, led to the formation of well-defined spherical clusters with interconnected chains, particularly for Bi576. This sample exhibited a highly porous and complex structure that increased the active surface area and facilitated electrolyte diffusion, which are favorable features for PEC applications. Overall, both the pulse electrodeposition technique and the $VO(acac)_2$ volume played decisive roles in determining the final $BiVO_4$ morphology. Pulse deposition enabled finer control of nucleation and grain connectivity, as demonstrated by the superior microstructure of Bi57 and the derived $BiVO_4$ film. Meanwhile, a sufficient amount of $VO(acac)_2$ ensured complete reaction and crystal growth, leading to dense and porous architectures. The synergistic effect of the optimized deposition conditions and precursor content resulted in a highly porous and interconnected Bi576 photoanode, which correlated well with its enhanced photoelectrochemical performance.

The TEM and HRTEM images of the Bi576 photoanode (Fig. 4k and l) further validate the crystallographic features suggested by XRD. Clear lattice fringes with an interplanar spacing of 0.309 nm can be observed, which are indexed to the (121) plane of monoclinic $BiVO_4$ (JCPDS No. 14-0688). This direct lattice-resolved evidence is consistent with the enhanced (121) diffraction peak intensity detected in the XRD pattern, confirming the preferential orientation along the (121) plane.

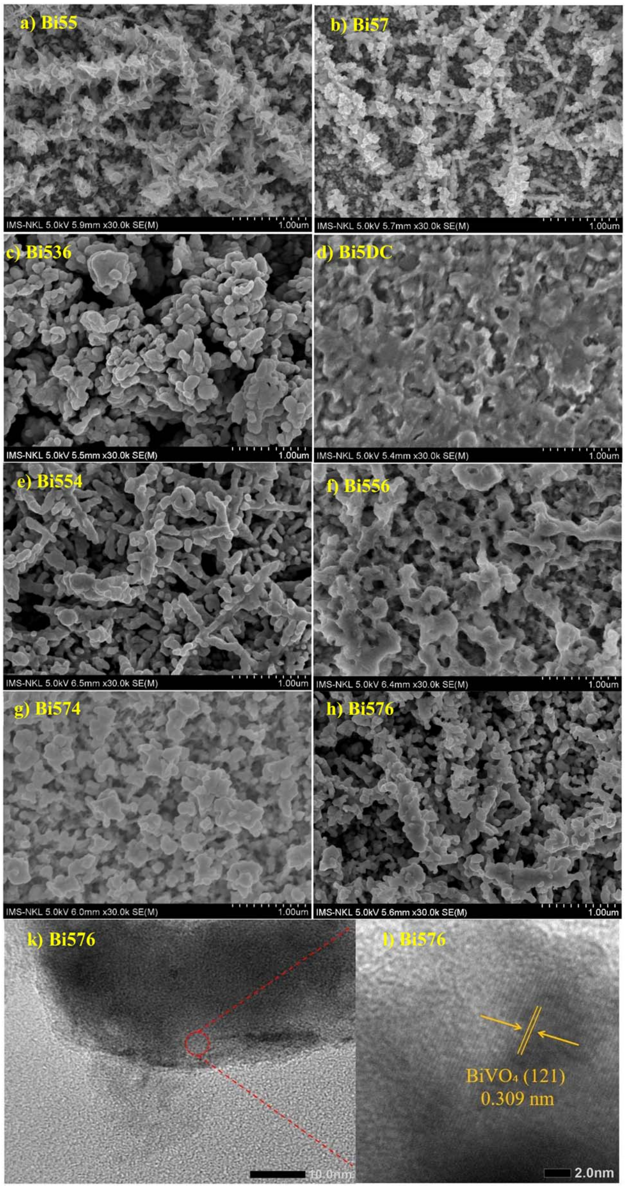

Fig. 4 FESEM images of bismuth metal films (a) Bi55, (b) Bi57, and (c) Bi536, (d) Bi5DC, (e) Bi554, (f) Bi556, (g) Bi574, and (h) Bi576 photoanodes, and (k) TEM and (l) HRTEM images of the Bi576 photoanode.

Such orientation is known to facilitate efficient charge separation and migration by reducing carrier recombination pathways. The combination of structural ordering, porous morphology, and orientation control accounts for the superior η_{inj} and photocurrent density achieved by the Bi576 electrode. Therefore, the HRTEM results provide strong microstructural support for the correlation between the crystal orientation and the remarkable PEC activity observed.

Linear sweep voltammetry (LSV) measurements (Fig. 5a) were conducted to assess the photoelectrochemical (PEC) water-splitting performance of the $BiVO_4$ photoanodes in 0.5 M Na_2SO_4 solution (pH $\approx$ 6.5) under AM 1.5G illumination (100 mW cm^{-2}). The photocurrent density at 1.23 V *vs.* RHE followed the increasing order: Bi5DC < Bi536 < Bi574 < Bi554 < Bi556 < Bi576, corresponding to 0.21, 0.50, 0.74, 0.78, 1.04, and 1.33 mA cm^{-2}, respectively. This trend clearly demonstrates that the Bi576 sample exhibited the highest PEC activity. The superior performance of Bi576 can be attributed to a combination of favorable structural and morphological features. XRD analysis revealed a dominant (121) crystallographic orientation, which facilitated anisotropic charge transport and reduced bulk recombination. Raman spectroscopy confirmed enhanced V–O bonding with a shorter bond length, indicative of improved orbital overlap and electronic conductivity. Additionally, the FESEM images show a highly porous, interconnected morphology that increases the electrochemical active surface area and promotes efficient charge transfer at the electrode–electrolyte interface. Importantly, the improved PEC performance of Bi576 also correlated with the precise control of the pulse electrodeposition parameters and optimal amount of the $VO(acac)_2$ precursor. These synergistic factors enhance the structural integrity and surface complexity of the film, leading to superior light absorption, charge separation, and photocatalytic activity. This confirms the critical role of the deposition strategy and precursor design in optimizing $BiVO_4$-based photoanodes for solar water-splitting applications.

Using sulfite oxidation as a kinetic benchmark, the Bi576 photoanode exhibits a surface charge transfer efficiency $\eta_{\text{inj}} = \eta_{\text{transfer}} = 60.1\%$ at 1.23 V_{RHE}, outperforming Bi574 (43.3%) and Bi556 (33.2%), as shown in Table 1. The bulk charge separation efficiency reaches $\eta_{\text{sep}} = 29.5\%$ at the same bias, yielding an overall $\eta_{\text{overall}} = \eta_{\text{sep}} \times \eta_{\text{inj}} = 17.7\%$. These values, obtained under AM 1.5G illumination in neutral 0.5 M Na_2SO_4 and computed following recent protocols,[28–30] confirm that the superior PEC activity of Bi576 arises from both efficient bulk charge separation and markedly enhanced interfacial transfer.

The applied bias photon-to-current efficiency (ABPE), calculated from the LSV data (Fig. 5b), further confirmed the superior photoelectrochemical performance of the Bi576 photoanode in this study. Among all the samples, Bi576 exhibited the highest ABPE value of approximately 20% at a low bias voltage (below 0.8 V *vs.* RHE), underscoring its efficient solar-to-hydrogen conversion capability. The remarkable ABPE performance of Bi576 is attributed to the synergistic effect of improved crystallographic orientation, enhanced V–O bond strength, and a highly porous morphology. The higher vanadium precursor volume enabled a more complete reaction between the Bi and V species during annealing, contributing to improved charge separation and reduced surface recombination. These attributes allowed Bi576 to utilize photogenerated charge carriers more efficiently, translating into a greater applied bias efficiency. This result highlights how tuning the deposition parameters and precursor chemistry can effectively modulate the internal electric field and surface reactivity of $BiVO_4$ films, both of which are essential for maximizing the PEC efficiency under solar irradiation.

Electrochemical impedance spectroscopy (EIS) was performed to investigate the interfacial charge transfer dynamics at the electrode–electrolyte interface under illumination (Fig. 5c). The Nyquist plots revealed semicircles of varying diameters, from which the charge-transfer resistance (R_{ct}) was extracted.

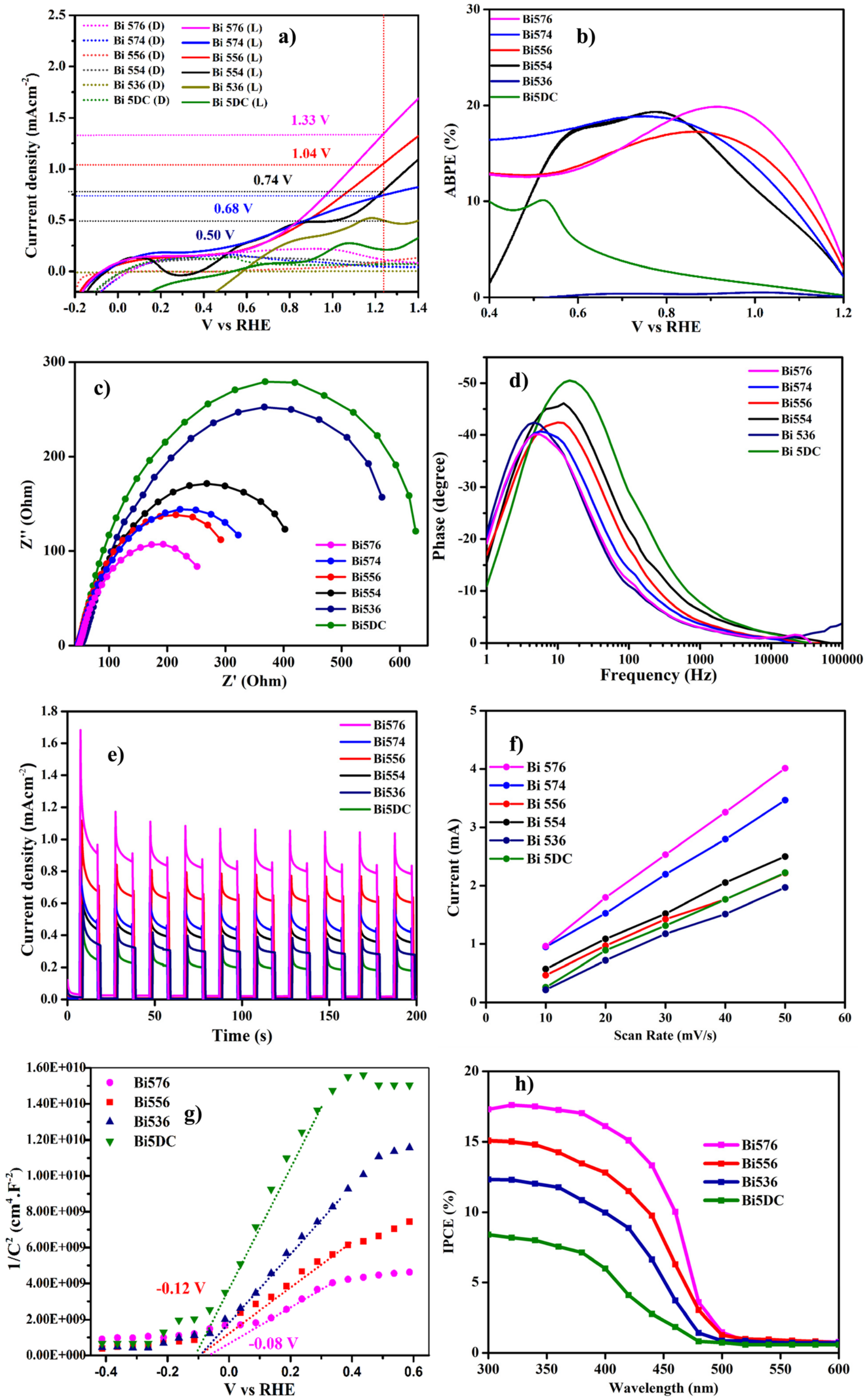

Fig. 5 (a) LSV curves in the dark and under light illumination, (b) ABPE curves, (c) EIS curves, (d) Bode curves, (e) transient photocurrent curves, and (f) ECSA evaluation of Bi576, Bi574, Bi556, Bi554, Bi536, and Bi5DC photoanodes. (g) Mott–Schottky plots of Bi-576, Bi556, Bi536, and Bi5DC photoanodes. (h) ICPE plots of Bi-576, Bi-556, Bi536, and Bi5DC photoanodes.

The Bi576 sample exhibited the smallest semicircle, indicating the lowest R_{ct} among all the photoanodes, whereas Bi5DC and Bi536 showed much larger semicircles, corresponding to higher interfacial resistance. The lower R_{ct} value of Bi576 is a direct consequence of its interconnected porous morphology, which provides abundant reaction sites and facilitates faster ion

Table 1 Photoelectrochemical parameters of Bi5DC, Bi536, Bi554, Bi556, Bi574, and Bi576 photoanodes

Samples	$J \sim 1.23$ V (mA)	Onset potential (V_{RHE})	ABPE (%)	C_{dl} (μFcm^{-2})	ECSA	R_{ct}	t (ms)	N (cm^{-3})	η_{inj} (%)	η_{sep} (%)
Bi5DC	0.21	0.55	0.64	38.00	512	256.60	10.04	2.66×10^{20}	27.20	10.39
Bi536	0.50	0.64	1.24	43.00	538	124.00	12.04	3.58×10^{20}	31.20	21.4
Bi554	0.68	0.55	16.80	48.00	600	256.60	15.66		39.11	22.14
Bi556	1.04	0.82	14.80	48.20	598	142.00	13.42	5.77×10^{20}	33.18	41.83
Bi574	0.74	0.27	16.30	63.19	790	92.15	29.91		43.33	22.73
Bi576	1.33	0.60	20.00	75.74	947	82.79	31.46	8.65×10^{20}	60.10	29.46

diffusion and charge transport kinetics. Additionally, the improved structural ordering and V–O bond strength enhance the electronic conductivity, reducing the resistance to charge injection at the semiconductor/electrolyte interface. These findings are consistent with the LSV and ABPE results and reinforce the conclusion that optimized pulse electrodeposition, coupled with sufficient vanadium precursor loading, is essential for producing $BiVO_4$ photoanodes with excellent charge-transfer characteristics and PEC performance.

Bode phase plots (Fig. 5d) were analyzed to estimate the interfacial time constant (τ_{int}) on the $BiVO_4$ surface, which reflects the kinetics of the interfacial charge transfer. The (τ_{int}) increased in the following order: Bi5DC < Bi536 < Bi574 < Bi554 < Bi556 < Bi576, with Bi576 achieving the highest lifetime of 31.46 ms. A longer interfacial time constant implies slower recombination kinetics and prolonged charge carrier availability for participation in the oxygen evolution reaction (OER). This significant improvement in Bi576 originates from its well-organized crystal structure and highly porous interconnected network, which collectively reduce trap-assisted recombination. Moreover, enhanced phase purity and reduced defect density, as shown by Raman spectroscopy, further support efficient hole transport to the electrolyte interface. The prolonged carrier lifetime is directly correlated with a higher photocurrent density and ABPE, reinforcing the critical role of both crystallographic and morphological optimizations in PEC performance.

Transient photocurrent measurements (Fig. 5e) were performed under chopped AM 1.5G illumination to evaluate the photostability and responsiveness of the $BiVO_4$ photoanodes. Among all the samples, Bi576 exhibited the most stable and repeatable photocurrent response with minimal current decay during successive light on/off cycles. This behavior is indicative of the efficient separation and transport of photogenerated charge carriers, as well as low recombination rates at the surface. The robust transient response of Bi576 can be attributed to its optimized morphology and superior crystallinity. The interconnected porous structure enhances charge carrier collection, while the reduced structural defects, confirmed by Raman and XRD analyses, limit recombination at the grain boundaries. Moreover, the stronger V–O orbital interactions, as suggested by the blue-shifted Raman peak, contributed to better electronic conductivity and sustained photocurrent output under illumination. This photostability highlights the reliability of Bi576 for long-term PEC operation and confirms that rationally tuned electrodeposition conditions not only improve the performance but also enhance the durability of the device.

The electrochemical active surface area (ECSA) of the $BiVO_4$ photoanodes was estimated from cyclic voltammetry (CV) curves (Fig. S1) using the double-layer capacitance (C_{dl}) method (Fig. 5f). Bi576 exhibited the highest C_{dl} value (75.74 μF cm^{-2}), corresponding to the largest ECSA among all the samples. This indicates a greater density of electrochemically accessible sites, which is essential for facilitating surface redox reactions, such as water oxidation. The enhanced ECSA of Bi-576 stems from its hierarchical surface morphology, which is composed of porous, interconnected nanostructures. These features increase the contact area with the electrolyte and promote efficient charge transfer, consistent with the low R_{ct} from EIS and high photocurrent from LSV. Collectively, the increased ECSA, prolonged interfacial time constant, and strong transient photocurrent stability confirm that Bi576 benefits from a synergistic enhancement of both bulk and interfacial charge dynamics, directly contributing to its superior PEC water-splitting performance.

The Mott–Schottky (MS) plots of the $BiVO_4$ photoanodes (Fig. 5g) were measured at a frequency of 1 kHz in 1 M KOH electrolyte under dark conditions. All the samples exhibited positive slopes in the linear region, confirming their n-type semiconductor characteristics. The flat band potentials (V_{fb}) were estimated by extrapolating the linear portions of the plots to the *x*-axis, yielding approximate values of −0.08 V for Bi-576 and −0.12 V for Bi-556, respectively. These relatively negative (V_{fb}) values are favorable for photoelectrochemical water oxidation because they enhance band bending and charge separation at the semiconductor–electrolyte interface.

In addition to V_{fb}, the donor density N_{d}—an important parameter reflecting the majority carrier concentration—was calculated from the Mott–Schottky equation:

$$\frac{1}{C^2} = \frac{2}{eN_{\mathrm{d}}\varepsilon_0\varepsilon_{\mathrm{r}}}\left(V - V_{\mathrm{fb}} - \frac{KT}{e}\right)$$

where C, e, $\mathrm{N_d}$, ε_0, ε_{r}, V, V_{fb}, K, and T represent the space charge capacitance (F cm^{-2}), electron charge (1.6×10^{-19} C), carrier concentration, vacuum permittivity (8.86×10^{-12} F m^{-1}), relative permittivity for $BiVO_4$ (68 F m^{-1}), applied bias voltage, flat band potential, Boltzmann constant (1.38×10^{-23} J K^{-1}), and absolute temperature, respectively.

From the slopes of the linear region in the MS plot, N_{d} can be determined using the rearranged form as follows:

$$N_\mathrm{d} = \frac{2}{e\varepsilon_0\varepsilon_\mathrm{r}}\left(\frac{\mathrm{d}\left(\frac{1}{C^2}\right)}{\mathrm{d}V}\right)^{-1}$$

Bi-576 exhibited the smallest slope, indicating the highest donor density among the tested samples. This higher N_d contributes to improved electrical conductivity and enhanced charge transport within the photoanode. Conversely, the steeper slopes observed for Bi-536 and Bi-5DC imply lower carrier concentrations, which can limit the PEC performance owing to poorer charge transport properties. The combination of a more favorable flat band potential and higher donor density in Bi-576 underscores its superior electronic structure, which further explains its enhanced photocurrent and ABPE values. These Mott–Schottky results are consistent with the EIS, transient photocurrent, and LSV analyses, confirming the critical role of tailored electrodeposition in tuning the semiconductor properties of $BiVO_4$ photoanodes.

Table 2 summarizes the PEC performance of single-layer $BiVO_4$ electrodes prepared by mainstream methods under comparable AM 1.5G testing conditions. SILAR-prepared films can deliver relatively high photocurrents (*e.g.*, ~1.9 mA cm^{-2} at 1.23 V_{RHE} in ref. 31), but such approaches often require multiple deposition–annealing cycles and face scalability challenges. Spin-coated/sol–gel films (ref. 1) and spray-pyrolyzed films (ref. 35) generally report lower photocurrents of ~0.6–1.0 mA cm^{-2}, limited by poor charge separation and transport. Several electrodeposited $BiVO_4$ photoanodes achieve modest baseline

Table 2 Comparison of photoelectrochemical parameters of $BiVO_4$ electrodes fabricated by various methods

$BiVO_4$ preparation method	Photocurrent density @1.23 V_{RHE} (mA cm^{-2})	ABPE (%)	Stability	Electrolyte	Ref
SILAR (thin films, optimized cycles)	1.95	0.5–0.8	—	0.5 M Na_2SO_4 (pH 7)	31
SILAR (nanostructured $BiVO_4$)	1.2	~0.8	>1 h, >90% retained	0.5 M Na_2SO_4 (pH 7)	37
Electrodeposition (BiOI precursor → $BiVO_4$)	0.32	—	—	0.1 M KPi buffer (pH 7)	32
Electrodeposition (Bi metal → $BiVO_4$)	~1.1	0.15	>2 h, stable	0.1 M KPi buffer (pH 7)	33
Electrodeposition of $BiVO_4$	~1.0	—	Stable	0.5 M Na_2SO_4 (pH 7)	38
Reactive magnetron sputtering	2.1	0.4	—	0.5 M Na_2SO_4 (pH 7)	34
Spin coating	~0.8	0.06	—	0.5 M Na_2SO_4 (pH 7)	1
Atomic layer deposition	1.17	—	20% drop after 2 h	0.5 M Na_2SO_4	35
Spray pyrolysis	1.66	—	~5 min	0.5 M borate buffer (pH 9.5)	39
	0.58	—	—	0.5 M Na_2SO_4 (pH 7.2)	40
Hydrothermal synthesis	0.5			0.5 M Na_2SO_4 (pH 6.8)	36
	0.075			1 M KOH (pH 13.3)	41
Electrodeposition of $BiVO_4$	1.30	0.2	18% drop after 10 h	0.5 M Na_2SO_4 (pH 6.8)	This work

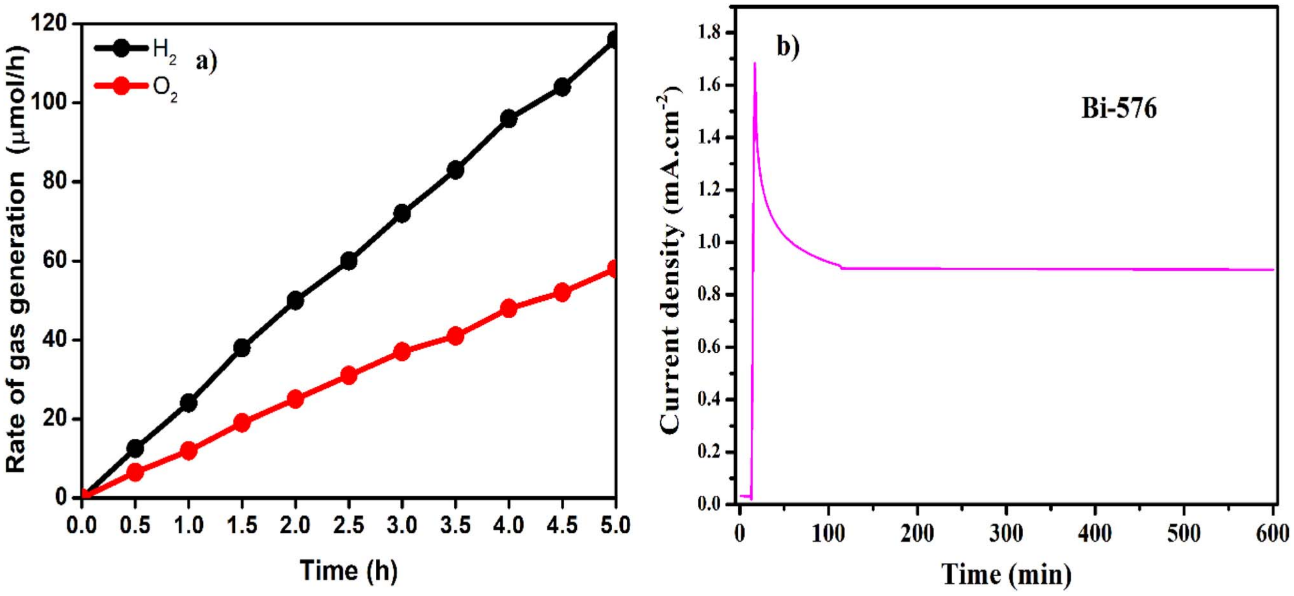

Fig. 6 (a) Hydrogen evolution and oxygen evolution–time curves of Bi-576 per area (1 cm^2) under AM 1.5G illumination. (b) Photostability tests (I–t curves at 1.23 V_{RHE}) over the Bi-576 photoanode.

values, such as 0.32 mA cm^{-2} (ref. 32), 0.61 mA cm^{-2} (ref. 35), and ~1.1 mA cm^{-2} (ref. 33), with ABPE values typically below 0.3% and η_{inj} <30%. Reactive magnetron sputtered $BiVO_4$ exhibits higher performance (≈2.1 mA cm^{-2} in 1 M K-borate, ref. 34), though still constrained by limited injection efficiency (~44%) and reliance on alkaline electrolytes. Atomic layer deposition (ALD, ref. 35) yields ~1.17 mA cm^{-2} in the phosphate + sulfite electrolyte, but the use of a sacrificial hole scavenger prevents direct benchmarking against water oxidation. Hydrothermally synthesized $BiVO_4$ (ref. 36) reports stable operation but with modest photocurrents (<2.0 mA cm^{-2}). In contrast, our optimized Bi576 electrode achieves a balanced and competitive

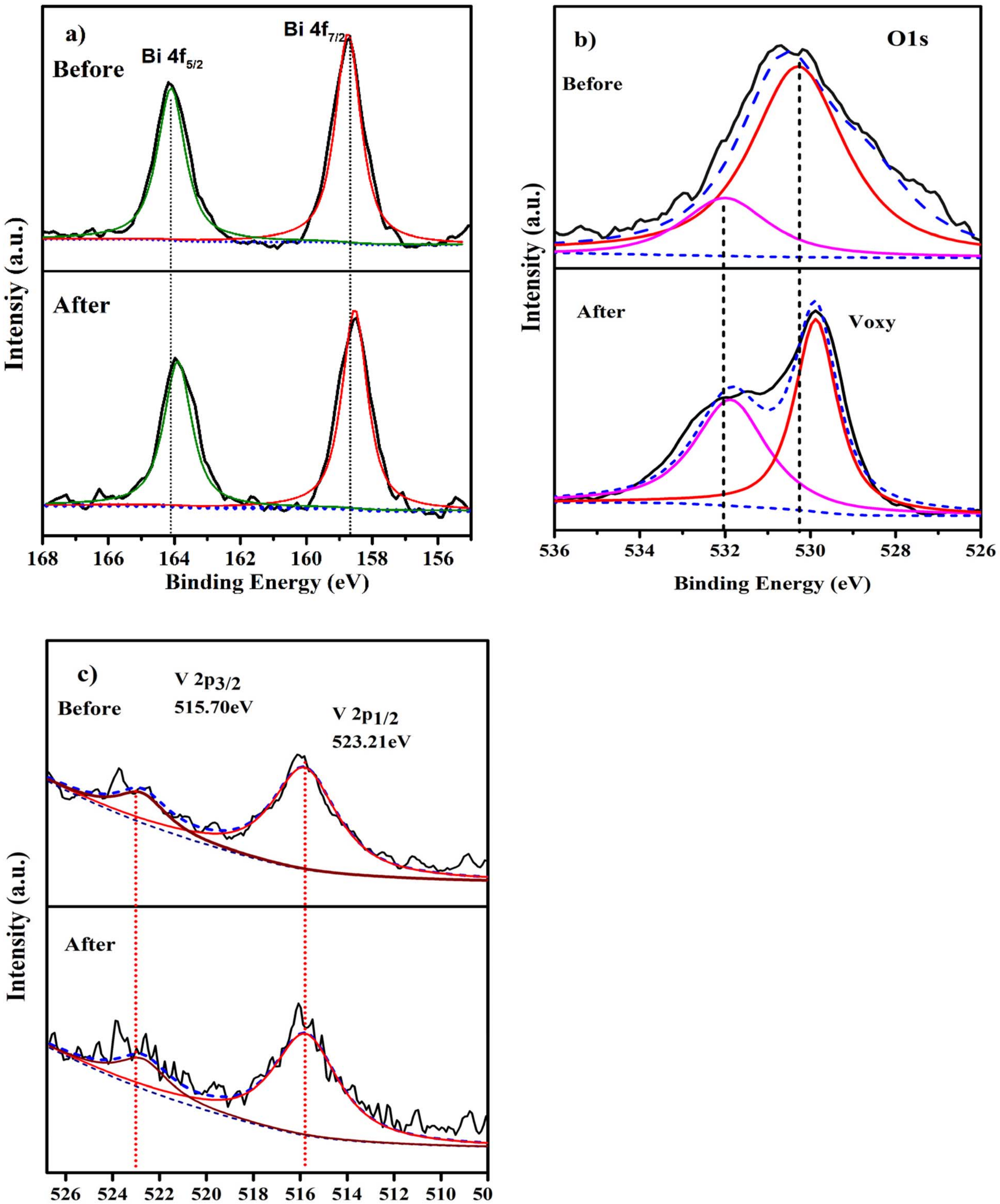

Fig. 7 High-resolution (a) Bi 4f, (b) O 1s, and (c) V 2p peaks of Bi-576 photoanode before and after PEC stability testing for 60 min (0.5 M Na_2SO_4).

performance in neutral electrolyte (0.5 M Na_2SO_4, pH $\approx$ 6.8): 1.30 mA cm^{-2} at 1.23 V_{RHE}, an ABPE of 20%, and a significantly higher η_{inj} of 60.1%. Compared with earlier electrodeposited films (η_{inj} typically 20–30%), this result highlights much more efficient interfacial charge transfer and reduced recombination. The performance advantage originates from our intensity-tuned pulse electrodeposition coupled with precursor-volume control, which produces (i) a porous interconnected morphology facilitating electrolyte infiltration, (ii) preferred (121) crystal orientation favoring charge transport, and (iii) an elevated donor density ($N_d \approx 8.65 \times 10^{20}$ cm^{-3}) that strengthens space-charge separation. Importantly, the work also verifies oxygen and hydrogen gas evolution and demonstrates >82% retention after 10 h of operation, which many literature reports lack. These structural and electronic optimizations enable more efficient utilization of photogenerated charges and position our approach among the most efficient and well-balanced single-layer $BiVO_4$ photoanodes synthesized by electrochemical methods to date, offering a practical and scalable pathway beyond ALD or sputtering while surpassing the efficiency and stability of conventional electrodeposited counterparts.

Fig. 6a shows the time-dependent gas evolution profiles of H_2 and O_2 over the Bi-576 photoanode under AM 1.5G illumination at 1.23 V *vs.* the RHE. The hydrogen generation rate steadily increased and reached approximately 115 μmol h^{-1} after 5 h, whereas the oxygen evolution rate followed a similar linear trend, reaching ~58 μmol h^{-1}. The observed $H_2:O_2$ molar ratio was close to the theoretical stoichiometric ratio of 2 : 1, confirming the high faradaic efficiency of the PEC process. These results validate that Bi576 can facilitate overall water splitting with excellent charge separation and utilization under continuous illumination. Fig. 6b illustrates the long-term photostability of Bi576 evaluated by chronoamperometry (*I–t*) at 1.23 V *vs.* RHE over 600 min of continuous illumination. The photocurrent density decreased slightly from ~1.45 to ~1.20 mA cm^{-2}, maintaining more than 82% of its initial value after 10 h. This slow degradation suggests strong structural stability and resistance to photocorrosion, which is likely attributed to the optimized crystal orientation, enhanced carrier concentration, and porous morphology that allow efficient charge transport and reduce surface degradation.

The surface chemical composition and oxidation states of the Bi-576 photoanode were further investigated using X-ray photoelectron spectroscopy (XPS), as shown in Fig. 6. The high-resolution Bi 4f spectrum (Fig. 7a) exhibits two characteristic peaks at 158.63 eV and 163.97 eV, corresponding to Bi 4f7/2 and Bi 4f5/2, respectively.[8,42] The ~5.34 eV spin-orbit splitting is consistent with the +3-oxidation state of bismuth (Bi^{3+}), confirming the correct incorporation of Bi into the $BiVO_4$ lattice. In the V 2p region (Fig. 7c), two distinct peaks located at 515.70 eV (V 2p3/2) and 523.21 eV (V 2p1/2) are observed, which correspond to the V^{5+} oxidation state.[43] The sharp and symmetric nature of these peaks indicates a well-crystallized and stoichiometric incorporation of vanadium, corroborating the Raman results that show strong V–O bonding and phase purity. The O 1s spectrum (Fig. 7b) is deconvoluted into two main components at 529.18 eV and 531.94 eV. The peak at 529.18 eV corresponds to lattice oxygen (O^{2-}) bound within the $BiVO_4$ structure, while the higher binding energy component at 531.94 eV is attributed to adsorbed hydroxyl groups (–OH) or surface oxygen species.[44] The presence of these surface oxygen species suggests potential surface defect states or functional groups that could act as active sites for water oxidation reactions. Such surface features can facilitate interfacial charge transfer and enhance photocatalytic performance. Taken together, the XPS results confirm the successful formation of $BiVO_4$ with the correct oxidation states of Bi^{3+} and V^{5+}, as well as the presence of beneficial surface oxygen species. These findings align well with the structural and electrochemical analyses, reinforcing the conclusion that the optimized pulse electrodeposition method and precursor volume not only improved the crystallinity and morphology but also fine-tuned the electronic structure of the photoanode. The strong V–O orbital interaction and appropriate surface chemistry collectively contribute to the excellent PEC performance and photostability of the Bi576 photoanode.

Conclusion

In this study, a highly efficient $BiVO_4$ photoanode was successfully fabricated *via* intensity-tuned pulse electrodeposition combined with controlled $VO(acac)_2$ precursor loading. Through a comprehensive structure–property–performance correlation, the Bi-576 sample emerged as the most promising candidate for solar-driven water splitting, achieving a high photocurrent density of 1.33 mA cm^{-2}, an ABPE of 20%, and an injection efficiency of 60.1% at 1.23 V *vs.* RHE. Among the fabricated samples, Bi-576 demonstrated superior photoelectrochemical (PEC) performance, achieving a photocurrent density of 1.33 mA cm^{-2} at 1.23 V *vs.* RHE, an applied bias photon-to-current efficiency (ABPE) of 20%, and a charge injection efficiency of 60.1%. These enhancements are attributed to a confluence of favorable factors, including a preferential (121) crystal orientation, reduced crystallite size, and a highly porous, interconnected morphology that collectively promote anisotropic charge transport and suppress bulk recombination. Raman and XPS analyses revealed stronger V–O orbital interactions and well-defined oxidation states (Bi^{3+} and V^{5+}), along with the presence of surface oxygen species, which contribute to improved charge separation and interfacial transfer kinetics. Electrochemical analyses further confirmed the high donor density (8.65×10^{20} cm^{-3}), prolonged interfacial time constant (31.46 ms), and low interfacial charge transfer resistance of Bi-576. Additionally, the photoanode maintained over 82% of its initial photocurrent after 10 hours of continuous operation, underscoring its structural and operational stability. These findings establish a clear link between deposition strategy, structural order, electronic configuration, and PEC functionality. The approach demonstrated here not only elevates $BiVO_4$ performance to a level comparable to more complex synthesis routes but also retains the simplicity, scalability, and cost-effectiveness of electrochemical fabrication. This work highlights the crucial role of interface and morphology engineering in developing next generation photoanodes for sustainable solar fuel production.

Author contributions

Nguyen Thi Huyen: methodology, writing – original draft; Thi Viet Ha Luu: data curation; Tran Le: data curation, writing – review & editing; Huu Phuc Dang: conceptualization, writing – review & editing.

Conflicts of interest

The authors declare that they have no competing financial interests or personal relationships that could influence the work reported in this study.

Data availability

Data for this article, including origin data, are available at (**https://doi.org/10.6084/m9.figshare.29512415**).

Supplementary information is available. See DOI: **https://doi.org/10.1039/d5na00667h**.

References

1 T. Zhou, S. Chen, J. Wang, Y. Zhang, J. Li, J. Bai and B. Zhou, Dramatically enhanced solar-driven water splitting of BiVO4 photoanode *via* strengthening hole transfer and light harvesting by co-modification of CQDs and ultrathin β-FeOOH layers, *Chem. Eng. J.*, 2021, **403**, 126350, DOI: **10.1016/j.cej.2020.126350**.

2 R. Li, X. Zhu, Q. Fu, G. Liang, Y. Chen, L. Luo, M. Dong, Q. Shao, C. Lin, R. Wei and Z. Guo, Nanosheet-based $Nb_{12}O_{29}$ hierarchical microspheres for enhanced lithium storage, *Chem. Commun.*, 2019, **55**, 2493–2496, DOI: **10.1039/C8CC09924C**.

3 B. Kang, M. Bilal Hussain, X. Cheng, C. Peng and Z. Wang, Green electrodeposition synthesis of NiFe-LDH/MoOx/BiVO4 for efficient photoelectrochemical water splitting, *J. Colloid Interface Sci.*, 2022, **626**, 146–155, DOI: **10.1016/j.jcis.2022.06.095**.

4 B. J. Trześniewski and W. A. Smith, Photocharged $BiVO_4$ photoanodes for improved solar water splitting, *J. Mater. Chem. A*, 2016, **4**, 2919–2926, DOI: **10.1039/C5TA04716A**.

5 K. Tian, L. Jin, A. Mahmood, H. Yang, P. An, J. Zhang, Y. Ji, Y. Li, D. Li, S. Frank) Liu and J. Yan, Lattice Distortion Promotes Carrier Separation to Improve the Photoelectrochemical Water Splitting Performance of Bismuth Vanadate Photoanode, *Adv. Funct. Mater.*, 2024, **34**, 2410548, DOI: **10.1002/adfm.202410548**.

6 Q. Bu, Y. Feng, B. Bai, J. Duan, Q. Mei, B. Bai and Q. Wang, Plasma-assisted photo-electrocatalysis in combination with Bi_5O_7I for efficient ammonia synthesis, *Catal. Sci. Technol.*, 2025, **15**, 2617–2627, DOI: **10.1039/D5CY00088B**.

7 J. Zhang, K. Chen, Y. Bai, L. Wang, J. Huang, H. She and Q. Wang, An MgO passivation layer and hydrotalcite derived spinel Co_2 AlO_4 synergically promote photoelectrochemical water oxidation conducted using $BiVO_4$-based photoanodes, *Nanoscale*, 2024, **16**, 10038–10047, DOI: **10.1039/D4NR00815D**.

8 N. A. Mohamed, H. Ullah, J. Safaei, A. F. Ismail, M. F. Mohamad Noh, M. F. Soh, M. A. Ibrahim, N. A. Ludin and M. A. Mat Teridi, Efficient Photoelectrochemical Performance of γ Irradiated g-C_3N_4 and Its g-C_3N_4 @$BiVO_4$ Heterojunction for Solar Water Splitting, *J. Phys. Chem. C*, 2019, **123**, 9013–9026, DOI: **10.1021/acs.jpcc.9b00217**.

9 N. A. Mohamed, N. A. Arzaee, M. F. Mohamad Noh, A. F. Ismail, J. Safaei, J. S. Sagu, M. R. Johan and M. A. Mat Teridi, Electrodeposition of BiVO4 with needle-like flower architecture for high performance photoelectrochemical splitting of water, *Ceram. Int.*, 2021, **47**, 24227–24239, DOI: **10.1016/j.ceramint.2021.05.134**.

10 H. Han, J. Seo, Y. Kim, J. Lee, J. Park, S. Yoon and B. Yoo, Electrodeposition of stress-relaxation-induced (111)-oriented nanotwin copper film by direct current in additive-free electrolyte, *Electrochim. Acta*, 2024, **475**, 143694, DOI: **10.1016/j.electacta.2023.143694**.

11 I. Fuentes-Camargo, J. E. Carrera-Crespo, J. Vazquez-Arenas, I. Romero-Ibarra, J. L. Rodríguez, L. Lartundo-Rojas and J. Cardoso-Martínez, Pulse-Plating Electrodeposition of Metallic Bi in an Organic-Free Aqueous Electrolyte and Its Conversion into $BiVO_4$ To Improve Photoelectrochemical Activity toward Pollutant Degradation under Visible Light, *J. Phys. Chem. C*, 2020, **124**, 1421–1428, DOI: **10.1021/acs.jpcc.9b09898**.

12 J. Vazquez-Arenas, T. Treeratanaphitak and M. Pritzker, Formation of Co–Ni alloy coatings under direct current, pulse current and pulse-reverse plating conditions, *Electrochim. Acta*, 2012, **62**, 63–72, DOI: **10.1016/j.electacta.2011.11.085**.

13 J. Zhao, Y. Peng, K. Yang, Y. Chen, S. Zhao and Y.-M. Liu, A new ratiometric fluorescence assay based on resonance energy transfer between biomass quantum dots and organic dye for the detection of sulfur dioxide derivatives, *RSC Adv.*, 2019, **9**, 41955–41961, DOI: **10.1039/C9RA09437G**.

14 C. L. P. Pavithra, B. V. Sarada, K. V. Rajulapati, T. N. Rao and G. Sundararajan, A New Electrochemical Approach for the Synthesis of Copper-Graphene Nanocomposite Foils with High Hardness, *Sci. Rep.*, 2014, **4**, 4049, DOI: **10.1038/srep04049**.

15 T. Senasu, S. Youngme, K. Hemavibool and S. Nanan, Sunlight-driven photodegradation of oxytetracycline antibiotic by BiVO4 photocatalyst, *J. Solid State Chem.*, 2021, **297**, 122088, DOI: **10.1016/j.jssc.2021.122088**.

16 K. Zhang, Y. Liu, J. Deng, S. Xie, X. Zhao, J. Yang, Z. Han and H. Dai, Co–Pd/BiVO4: High-performance photocatalysts for the degradation of phenol under visible light irradiation, *Appl. Catal., B*, 2018, **224**, 350–359, DOI: **10.1016/j.apcatb.2017.10.044**.

17 Q. Lu, L. Ding, J. Li, N. Wang, M. Ji, N. Wang and K. Chang, High transmittance BiVO4 thin-film photoanodes by reactive magnetron sputtering for a photovoltaic-photoelectrocatalysis water splitting system, *Int. J.*

Hydrogen Energy, 2024, **71**, 1142–1150, DOI: **10.1016/j.ijhydene.2024.04.168**.

18 L. Alexander and H. P. Klug, Determination of Crystallite Size with the X-Ray Spectrometer, *J. Appl. Phys.*, 1950, **21**, 137–142, DOI: **10.1063/1.1699612**.

19 P. Brack, J. S. Sagu, T. A. N. Peiris, A. McInnes, M. Senili, K. G. U. Wijayantha, F. Marken and E. Selli, Aerosol-Assisted CVD of Bismuth Vanadate Thin Films and Their Photoelectrochemical Properties, *Chem. Vap. Deposition*, 2015, **21**, 41–45, DOI: **10.1002/cvde.201407142**.

20 Z. Peng, Y. Su, I. Ennaji, A. Khojastehnezhad and M. Siaj, Encapsulation of few-layered MoS2 on electrochemical-treated BiVO4 nanoarray photoanode: Simultaneously improved charge separation and hole extraction towards efficient photoelectrochemical water splitting, *Chem. Eng. J.*, 2023, **477**, 147082, DOI: **10.1016/j.cej.2023.147082**.

21 S. Nikam and S. Joshi, Irreversible phase transition in BiVO $_4$ nanostructures synthesized by a polyol method and enhancement in photo degradation of methylene blue, *RSC Adv.*, 2016, **6**, 107463–107474, DOI: **10.1039/C6RA14700C**.

22 M. R. da S. Pelissari, N. F. Azevedo Neto, L. P. Camargo and L. H. Dall'Antonia, Characterization and Photo-Induced Electrocatalytic Evaluation for BiVO4 Films Obtained by the SILAR Process, *Electrocatalysis*, 2021, **12**, 211–224, DOI: **10.1007/s12678-021-00641-2**.

23 F. D. Hardcastle and I. E. Wachs, Determination of vanadium-oxygen bond distances and bond orders by Raman spectroscopy, *J. Phys. Chem.*, 1991, **95**, 5031–5041, DOI: **10.1021/j100166a025**.

24 D. L. Wood and J. Tauc, Weak Absorption Tails in Amorphous Semiconductors, *Phys. Rev. B*, 1972, **5**, 3144–3151, DOI: **10.1103/PhysRevB.5.3144**.

25 P. Hajra, S. Kundu, A. Maity and C. Bhattacharya, Facile photoelectrochemical water oxidation on Co^{2+}-adsorbed BiVO4 thin films synthesized from aqueous solutions, *Chem. Eng. J.*, 2019, **374**, 1221–1230, DOI: **10.1016/j.cej.2019.06.014**.

26 S. N. Haji Yassin, A. S. L. Sim and J. R. Jennings, Photoelectrochemical evaluation of SILAR-deposited nanoporous BiVO4 photoanodes for solar-driven water splitting, *Nano Mater. Sci.*, 2020, **2**, 227–234, DOI: **10.1016/j.nanoms.2019.10.003**.

27 J. Wang, Q. Ma, Y. Wei, Y. Guo, H. Li, H. Song, W. Sun and X. Li, BiVO4/CuIn5S8 heterojunction with rich sulphur vacancies for boosting visible light-driven photocatalytic water oxidation, *Mol. Catal.*, 2024, **561**, 114154, DOI: **10.1016/j.mcat.2024.114154**.

28 X. Chen, X. Li, Y. Peng, H. Yang, Y. Tong, M. -Sadeeq Balogun and Y. Huang, Tailoring Carrier Dynamics of $BiVO_4$ Photoanode *via* Dual Incorporation of Au and $Co(OH)_x$ Cooperative Modification for Photoelectrochemical Water Splitting, *Adv. Funct. Mater.*, 2025, **35**, 2416091, DOI: **10.1002/adfm.202416091**.

29 D. Li, X. Chen, M. Shao, S. Hou, J. Guo, H. Jin, H. Yang, G. Chen and Y. Huang, Metal–organic framework-derived nano-CoS-enhanced photoelectrochemical water splitting performance of the $BiVO_4$ photoanode, *J. Mater. Chem. A*, 2025, **13**, 22652–22659, DOI: **10.1039/D5TA02162F**.

30 Y. Chen, J. Huang, J. Zhou, X. Li, H. Yang and Y. Huang, Combinational effect of NiFeOx/Tb(OH)x as hole extractor for enhanced charges separation and stability of BiVO4 photoanode for solar water splitting, *Mater. Today Adv.*, 2025, **25**, 100554, DOI: **10.1016/j.mtadv.2024.100554**.

31 M. R. da S. Pelissari, N. F. Azevedo Neto, L. P. Camargo and L. H. Dall'Antonia, Characterization and Photo-Induced Electrocatalytic Evaluation for BiVO4 Films Obtained by the SILAR Process, *Electrocatalysis*, 2021, **12**, 211–224, DOI: **10.1007/s12678-021-00641-2**.

32 N. A. Mohamed, N. A. Arzaee, M. F. Mohamad Noh, A. F. Ismail, J. Safaei, J. S. Sagu, M. R. Johan and M. A. Mat Teridi, Electrodeposition of BiVO4 with needle-like flower architecture for high performance photoelectrochemical splitting of water, *Ceram. Int.*, 2021, **47**, 24227–24239, DOI: **10.1016/j.ceramint.2021.05.134**.

33 Y. Guan, X. Gu, Q. Deng, S. Wang, Z. Li, S. Yan and Z. Zou, Synergy Effect of the Enhanced Local Electric Field and Built-In Electric Field of CoS/Mo-Doped $BiVO_4$ for Photoelectrochemical Water Oxidation, *Inorg. Chem.*, 2023, **62**, 16919–16931, DOI: **10.1021/acs.inorgchem.3c02622**.

34 Q. Lu, L. Ding, J. Li, N. Wang, M. Ji, N. Wang and K. Chang, High transmittance BiVO4 thin-film photoanodes by reactive magnetron sputtering for a photovoltaic-photoelectrocatalysis water splitting system, *Int. J. Hydrogen Energy*, 2024, **71**, 1142–1150, DOI: **10.1016/j.ijhydene.2024.04.168**.

35 M. Stefik, Atomic Layer Deposition of Bismuth Vanadates for Solar Energy Materials, *ChemSusChem*, 2016, **9**, 1727–1735, DOI: **10.1002/cssc.201600457**.

36 S. S. Kalanur and H. Seo, An experimental and density functional theory studies of Nb-doped BiVO4 photoanodes for enhanced solar water splitting, *J. Catal.*, 2022, **410**, 144–155, DOI: **10.1016/j.jcat.2022.04.019**.

37 Q. Lu, L. Ding, J. Li, N. Wang, M. Ji, N. Wang and K. Chang, High transmittance BiVO4 thin-film photoanodes by reactive magnetron sputtering for a photovoltaic-photoelectrocatalysis water splitting system, *Int. J. Hydrogen Energy*, 2024, **71**, 1142–1150, DOI: **10.1016/j.ijhydene.2024.04.168**.

38 Y. Gao, W. Zhao, Z. Tian, L. Zhang, Z. Teng, N. Li and L. Ge, Cobalt-Modified Amorphous Nickel–Iron–Molybdate Cocatalysts to Enhance the Photoelectrochemical Water Splitting Performance of $BiVO_4$ Photoanodes, *ACS Appl. Energy Mater.*, 2023, **6**, 4342–4353, DOI: **10.1021/acsaem.3c00326**.

39 I. J. Madatta, Y. Liu, J. Ding, Z. Jian, Y. Xiong, W. Fan and W. Shi, High-Performing $BiVO_4$ Thin Films for Photoassisted Water Oxidation: A Scalable Ultrasonic Spray Pyrolysis Approach, *Ind. Eng. Chem. Res.*, 2025, **64**, 14364–14372, DOI: **10.1021/acs.iecr.5c01507**.

40 D. Wang, H. Wang, J. Fan, H. Zhu, A. Fujishima and X. Zhang, Nanocone-substrated BiVO4-Mo/MOFs photoanodes for highly efficient photoelectrochemical

water splitting, *Int. J. Hydrogen Energy*, 2024, **68**, 596–606, DOI: 10.1016/j.ijhydene.2024.04.317.

41 A. Pandiaraj, M. M. Ibrahim, K. Jothivenkatachalam and V. Kavinkumar, Photoelectrochemical Water Splitting Over Decahedron Shaped BiVO4 Photoanode by Tuning the Experimental Parameters, *J. Cluster Sci.*, 2023, **34**, 557–564, DOI: 10.1007/s10876-022-02236-3.

42 W. Bai, Y. Zhou, G. Peng, J. Wang, A. Li and P. F.-X. Corvini, Engineering efficient hole transport layer Ferrihydrite-MXene on BiVO4 photoanodes for photoelectrochemical water splitting: Work function and conductivity regulated, *Appl. Catal., B*, 2022, **315**, 121606, DOI: 10.1016/j.apcatb.2022.121606.

43 N. A. Mohamed, J. Safaei, A. F. Ismail, M. N. Khalid, M. F. A. Mohd Jailani, M. F. M. Noh, N. A. Arzaee, D. Zhou, J. S. Sagu and M. A. M. Teridi, Boosting photocatalytic activities of BiVO4 by creation of g-C3N4/ZnO@BiVO4 Heterojunction, *Mater. Res. Bull.*, 2020, **125**, 110779, DOI: 10.1016/j.materresbull.2020.110779.

44 Y. Li, Y. Liu, Y. Hao, X. Wang, R. Liu and F. Li, Fabrication of core-shell BiVO4@Fe2O3 heterojunctions for realizing photocatalytic hydrogen evolution *via* conduction band elevation, *Mater. Des.*, 2020, **187**, 108379, DOI: 10.1016/j.matdes.2019.108379.